

Novel heating/cooling stage designed for fluid inclusion microthermometry of large stalagmite sections

Article

Accepted Version

Krüger, Y., Hiltbrunner, B., Luder, A., Fleitmann, D. and Frenz, M. (2014) Novel heating/cooling stage designed for fluid inclusion microthermometry of large stalagmite sections. *Chemical Geology*, 386. pp. 59-65. ISSN 0009-2541 doi: <https://doi.org/10.1016/j.chemgeo.2014.08.004> Available at <https://centaur.reading.ac.uk/40202/>

It is advisable to refer to the publisher's version if you intend to cite from the work. See [Guidance on citing](#).

Published version at: <http://dx.doi.org/10.1016/j.chemgeo.2014.08.004>

To link to this article DOI: <http://dx.doi.org/10.1016/j.chemgeo.2014.08.004>

Publisher: Elsevier

All outputs in CentAUR are protected by Intellectual Property Rights law, including copyright law. Copyright and IPR is retained by the creators or other copyright holders. Terms and conditions for use of this material are defined in the [End User Agreement](#).

www.reading.ac.uk/centaur

CentAUR

Central Archive at the University of Reading

Reading's research outputs online

Novel heating/cooling stage designed for fluid inclusion microthermometry of large stalagmite sections

Yves Krüger^{1,4,*}, Beat Hiltbrunner², Andres Luder¹, Dominik Fleitmann^{3,4,5}, Martin Frenz¹

¹Institute of Applied Physics, University of Bern, Switzerland

²Astronomical Institute, University of Bern, Switzerland

³Institute of Geological Sciences, University of Bern, Switzerland

⁴Oeschger Centre for Climate Change Research, University of Bern, Switzerland

⁵present address: Department of Archaeology, School of Archaeology, Geography and Environmental Sciences, University of Reading, United Kingdom

Abstract

Liquid–vapour homogenisation temperatures of fluid inclusions in stalagmites are used for quantitative temperature reconstructions in paleoclimate research. Specifically for this application, we have developed a novel heating/cooling stage that can be operated with large stalagmite sections of up to $17 \times 35 \text{ mm}^2$ to simplify and improve the chronological reconstruction of paleotemperature time-series. The stage is designed for use of an oil immersion objective and a high-NA condenser front lens to obtain high-resolution images for bubble radius measurements. The temperature accuracy of the stage is better than $\pm 0.1 \text{ }^\circ\text{C}$ with a precision (reproducibility) of $\pm 0.02 \text{ }^\circ\text{C}$.

Keywords: microthermometry, heating stage, stalagmites, homogenisation temperature, paleotemperature

1. Introduction

During past decades stalagmites have become an important archive providing information on natural climate variations in the past (*e.g.* Fairchild *et al.*, 2006; Lachniet, 2009; McDermott *et al.*, 2004). Stalagmites can grow continuously over thousands of years by precipitation of calcite from the cave drip water and their age can precisely be dated using the uranium-series dating method. In weakly ventilated caves, the cave air temperature is nearly constant throughout the year and is closely related to the mean annual surface temperature outside the cave (Wigley and Brown, 1976). Thus, stalagmite formation temperatures can be used to develop time series of paleotemperature variations. In recent

* corresponding author:

e-mail: yves.krueger@iap.unibe.ch

phone: +41 (0)31 631 37 09

address: Sidlerstraße 5, CH-3012 Bern

Field Code Changed

35 years, different temperature proxies have been proposed to determine the formation
36 temperatures of stalagmites: (i) the combination of δD and $\delta^{18}O$ of fluid inclusion water and
37 speleothem calcite, respectively (e.g. Schwarcz *et al.*, 1976; McGarry *et al.*, 2004; Vonhof *et*
38 *al.*, 2006; Zhang *et al.*, 2008; Affolter *et al.*, 2014), (ii) the excess of ^{13}C - ^{18}O containing
39 molecules (so-called ‘clumped isotopes’) of calcite (Ghosh *et al.*, 2006; Affek *et al.*, 2008),
40 and (iii) the concentration of dissolved noble gases in the fluid inclusion water (Kluge *et al.*,
41 2008; Scheidegger *et al.*, 2010).

42 Recently, we have evaluated the applicability of fluid inclusion liquid–vapour
43 homogenisation temperatures as an alternative approach to determine stalagmite formation
44 temperatures (Krüger *et al.*, 2011). The method relies on the measurement of the temperature
45 at which a two-phase liquid–vapour inclusion homogenises to a stable monophasic liquid state
46 upon collapse of the vapour bubble. The temperature of the bubble collapse, i.e., the observed
47 homogenisation temperature $T_{h(obs)}$ depends on the density of the encapsulated drip water and
48 on the volume of the fluid inclusion. $T_{h(obs)}$ can be measured using a microscope
49 heating/cooling stage. Prior to measuring liquid–vapour homogenisation temperatures in
50 stalagmites, however, the initially monophasic liquid inclusions have to be transferred to a
51 stable two-phase system by applying single ultra-short laser pulses to stimulate vapour bubble
52 nucleation in the metastable liquid (Krüger *et al.*, 2007). Since stalagmites grow under
53 atmospheric pressure conditions, the density of the water preserved in the inclusions depends
54 only on the calcite formation temperature. By applying a thermodynamic model that accounts
55 for the effect of surface tension on liquid–vapour homogenisation (Marti *et al.*, 2012) the
56 density of the encapsulated drip water and hence the formation temperature of the stalagmite
57 can be calculated based on the measurement of $T_{h(obs)}$ and at least one additional measurement
58 of the vapour bubble radius at a known temperature. Previous studies on recent fluid
59 inclusions from the top part of actively growing stalagmites revealed a potential accuracy of
60 this new temperature proxy of approximately ± 0.2 °C (Krüger *et al.*, 2011).

61

62 **2. Motivation to develop a novel heating/cooling stage**

63

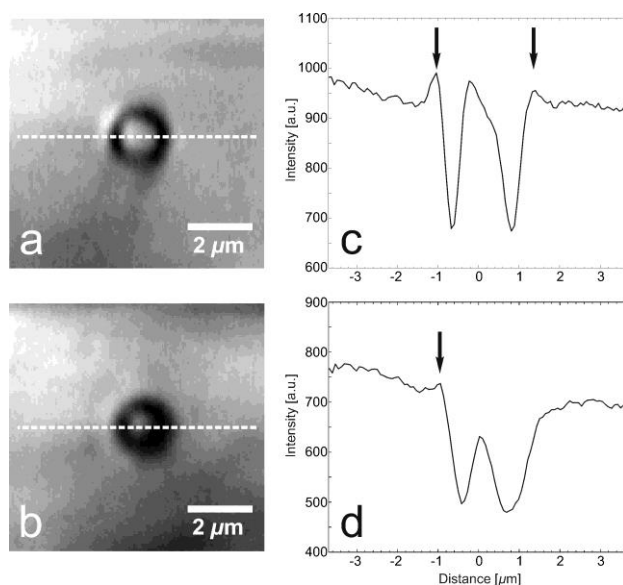
64 Fluid inclusions in stalagmites form during crystal growth (Kendall and Broughton,
65 1978) and are typically arranged along calcite growth bands. Thus, the inclusions and the
66 surrounding host calcite have the same age, which allows for a precise chronological
67 reconstruction of stalagmite formation temperatures determined from fluid inclusions. In
68 previous studies performed on a conventional Linkam THMSG 600 heating/freezing stage the

69 chronological reconstruction of the temperature data was complicated due to the fact that the
70 maximum sample size is limited to 7 mm in diameter. Hence, the initially ca. $20 \times 35 \text{ mm}^2$
71 large and 300–400 μm thick stalagmite sections had to be broken into smaller pieces after
72 removing them from the carrier glass that is needed to stabilize the sample during cutting.
73 This means a considerable and time-consuming effort for sample documentation prior to
74 microthermometric measurements. Nevertheless a precise reconstruction of the sections often
75 failed when the sample fractured to tiny pieces upon dissolving the glue (cyanoacrylate) in an
76 acetone bath. Therefore, the main motivation to build a new heating/cooling stage was to be
77 able to examine entire stalagmite sections that no longer need to be removed from the carrier
78 glass but remain fixed on a 0.3 mm thick glass substrate with $28 \times 48 \text{ mm}^2$ standard
79 dimensions.

80 The second reason to design a new stage was the application of a microscope objective and a
81 condenser front lens with high numerical apertures (NA) to improve the optical resolution and
82 the quality of the vapour bubble images that are used for determining the bubble radius
83 (Spadin et al., in prep.). The bubble images are taken with a CCD camera at known sub-
84 ambient temperatures: commonly at 5.1 °C, when the bubble radius reaches its maximum
85 (Marti et al., 2009). Since conventional heating/freezing stages like the Linkam THMSG 600
86 allow for microthermometric measurements from –180 up to 600 °C, their design requires the
87 application of long working distance (LWD) optics that, however, exhibit lower numerical
88 apertures than objectives and condenser front lenses with short working distances. For
89 example, the Olympus LMPlanFL 100x LWD objective we use for the Linkam stage has a
90 NA of 0.8, while the condenser front lens with a working distance of approximately 13 mm
91 has a NA of approximately 0.4. For the new heating/cooling stage that was designed for
92 applications in a narrow temperature range between –15 and 35°C, we wanted to use a 1.3
93 NA oil immersion objective (Olympus UPLFLN 100x) and a dry short working distance
94 condenser front lens with a NA of 0.9. The application of an oil immersion objective suggests
95 itself due to the fact that we do not polish the stalagmite sections but instead, we use
96 immersion oil to reduce light scattering at the rough surfaces and thus make the sections
97 transparent for microscopic observations in transmission. To illustrate the improvements of
98 the image quality and resolution, Fig. 1 shows a comparison of two microphotographs of the
99 same vapour bubble taken with the new (Fig. 1a) and the old (Fig. 1b) system. In Fig. 1a the
100 bubble image shows a dark ring with high contrast, whereas in Fig. 1b the dark ring appears
101 much broader and blurred due to lower contrast. Based on a simple ray–tracing model, Spadin
102 et al. (in prep.) found that reflection of light at the bubble meniscus results in a bright ring

103 surrounding the dark one. The intensity of this bright ring depends on the NA of the objective,
104 which is illustrated in Fig. 1c for the oil immersion objective (NA 1.3) and in Fig. 1d for the
105 LWD objective (NA 0.8). The intensity profile in Fig. 1c displays two distinct intensity
106 maxima outside the dark ring, whereas in Fig. 1d the two peaks can hardly be distinguished
107 from the background. In Fig. 1a and 1b the bright outer ring is only partially visible, which is
108 likely due to shadow effects occurring in the stalagmite section and resulting in a non-uniform
109 illumination of the vapour bubble.

110 An additional advantage of the oil immersion objective compared to the LWD objective is the
111 smaller focal spot size due to the higher numerical aperture and a significantly higher
112 transmission of the 800 nm laser wavelength emitted from the Ti:sapphire femtosecond (fs)
113 laser that is used to induce bubble nucleation. This means that for a given energy and duration
114 of the fs-laser pulse, the oil immersion objective provides a much higher pulse intensity in the
115 focus than the LWD objective, and in consequence, allows us to induce vapour bubble
116 nucleation in inclusions that are located up to 250 μm below the sample surface.



117
118 Fig. 1: Comparison of bubble images: a) microphotograph using a 100x oil immersion
119 objective (NA 1.3) and a condenser NA of 0.9. b) microphotograph using a 100x LWD
120 objective (NA 0.8) and a condenser NA of 0.4. c) and d) intensity profiles along the dashed
121 lines indicated in a) and b). Arrows indicate the intensity maximum of the outer bright ring.
122

123 3. Design of the heating/cooling stage

124

125 In the following we describe the design of the novel heating/cooling stage that is

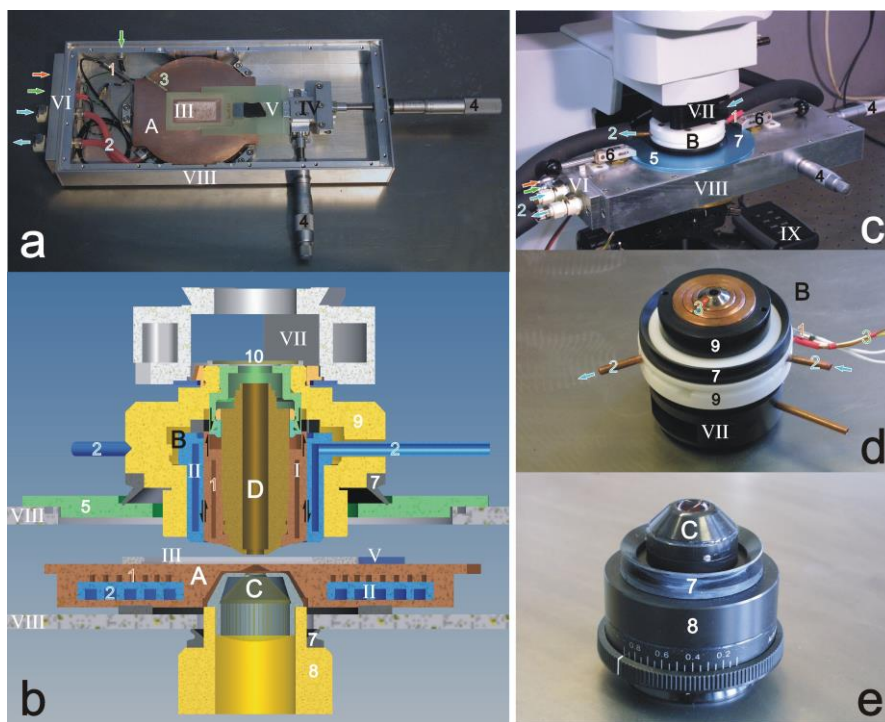
126 illustrated in Fig. 2a–e. All components described in the text are labelled in the figures
127 accordingly. The heating/cooling stage is mounted on a Olympus BX51 microscope (Fig. 2c)
128 and its dimensioning complies with the requirements set by the large sample size and the
129 short working distances of the microscope optics. To meet these demands we constructed a
130 large-sized (\varnothing 116 mm) heating/cooling block (A) made from copper, a material with
131 excellent thermal conductivity. The rear side of this copper block features a central recess to
132 bring the condenser front lens (C) close to the sample (Fig. 2b). The sample (III) is placed on
133 the top face of the block (Fig. 2a). The 0.9 NA condenser front lens used has a working
134 distance of \sim 3.5 mm and illuminates the sample through a tapered aperture with a final
135 diameter of 1.5 mm (Fig. 2b). The heating/cooling block (A) comprises (i) a sheathed twin-
136 core heating conductor (1; Thermocoax) of 1.7 m length and a diameter of 1.5 mm, which is
137 soldered in a spirally routed groove closely below to the surface (Fig. 2b); (ii) a cooling unit
138 (II) consisting of a cooling circuit (2) with inlet and outlet connections for the cooling liquid,
139 a water-ethylene glycol mixture. The cooling unit is placed below the heating conductor; (iii)
140 a Pt-100 thin-film temperature sensor (3; Heraeus) embedded in a slot on the top face of the
141 copper block (Fig. 2a).

142 The sample (III), i.e., the 0.3 mm carrier glass with the stalagmite section, is fixed in a 2 mm
143 thick fibreglass frame that prevents leakage of the immersion oil on the copper block (Fig.
144 2a). For the preparation of the sample we use UV curable epoxy resins that are inert against
145 the immersion oil and can be applied at sub-ambient temperatures. Prior to the cutting of the
146 sections, the stalagmite sample is fixed on the carrier glass using a low-viscous resin (Epo-
147 Tek OG603) that closely matches the refractive index of calcite ($n_e = 1.486$) in the cured state.
148 The carrier glass is then fixed to the bottom side of the fibreglass frame using a different,
149 higher viscous resin (Epo-Tek OG142). The fibreglass frame can be magnetically attached to
150 the sample holder (V) that is mounted on an x-y translation stage (IV). The translation stage is
151 moved by means of two micrometre gauges (4) with travel lengths of 50 mm and 25 mm,
152 respectively. The position of the sample can be read off from the scales on the micrometre
153 gauges, which allows for a precise localisation of the analysed fluid inclusions mandatory for
154 the chronological reconstruction of the temperature data. The maximum size of the stalagmite
155 sections that can be scanned with the oil immersion objective is $17 \times 35 \text{ mm}^2$.

156 The application of an immersion objective (D) that is in direct thermal contact with the
157 oil film covering the stalagmite sample requires an active control of the objective temperature
158 to minimise vertical temperature gradients and to achieve faster equilibration of the sample
159 temperature. Therefore, we have developed a copper heating/cooling jacket (B) that allows for

160 a precise regulation of the objective temperature. To accomplish an efficient heat transfer, the
161 heating/cooling jacket is attached directly to the inner brass cylinder that houses the objective
162 lenses (D). To this end, we removed the outer protective sleeve of the objective and modified
163 the spring system that protects the front lens from mechanical damage. The cylindrical
164 heating/cooling jacket consists of a heater element (I) that is made up of a coiled twin-core
165 heating conductor (1) embedded between two copper sleeves and an outer cooling unit (II)
166 with inlet and outlet connections (2) for the cooling liquid. The heater element (I) is screwed
167 on the objective (D) and features a 2 mm spring deflection relative to the cylindrical cooling
168 unit (II) that serves as guidance for the spring suspension of the objective. An insulating
169 sheath (9) made from Polyoxymethylene (POM), finally, encases the heating/cooling jacket.
170 The back aperture of the POM sheath is sealed with a 1 mm glass window (10) to prevent
171 condensation of moisture on the objective rear lens and within the heating/cooling jacket. The
172 whole assembly is fixed to the microscope frame by means of a detachable single-position
173 nosepiece (VII) with centring screws to align the objective to the optical axis. A lateral
174 through-hole (11, Fig. 2d) in the nosepiece can be used to flush the glass window with
175 nitrogen gas to remove the condensed air moisture from the glass window. The objective
176 temperature, finally, is measured by a Pt-100 thin-film sensor (3) that is placed close to the
177 objective front lens (Fig. 2d).

178 The sample chamber is placed inside a sealed off aluminium housing (VIII) to
179 minimise condensation of air moisture and thermal effects induced by air circulation. An
180 opening in the base plate (\varnothing 34 mm) provides access to enter the condenser front lens (C) and
181 is sealed off by a V-seal (7) mounted on the outer face of the adapter tube (8) that tightly
182 connects the aperture diaphragm and the front lens of the condenser (Fig. 2e). From above,
183 the objective with the heating/cooling jacket can be entered through an opening (\varnothing 60 mm) in
184 the centre of the detachable cover plate (5). A V-seal (7) mounted on the POM insulation
185 sheath seals off the port when the objective comes close to the sample. The cover plate is
186 fixed to the housing by means of two clamping levers (6) and thus can be easily and quickly
187 removed to load the sample. Finally, a plug board (VI) in the side wall of the aluminium
188 housing is used as lead-through to connect the lower heating/cooling block (A) to the electric
189 and the hydraulic circuits (Fig. 2a,c).



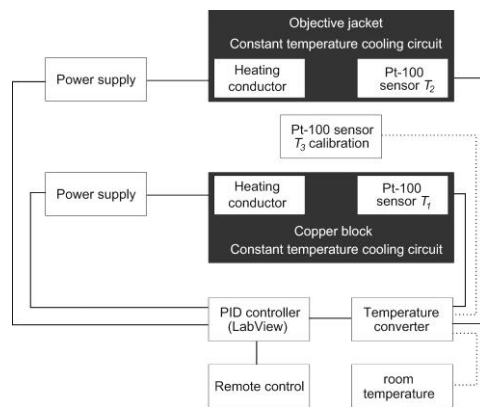
190
 191
 192 Fig. 2: a) View of the heating/cooling stage with removed cover b) Cross-section through the stage and the
 193 objective heating/cooling jacket c) stage mounted on the microscope d) objective with heating/cooling jacket e)
 194 condenser assembly.

195 Legend:
 196 A: heating/cooling block B: objective heating/cooling jacket C: condenser lens D: oil immersion objective.
 197 I: heater element II: cooling element III: sample IV: x-y translation stage V: sample holder VI: plug board VII:
 198 objective nose piece VIII: stage housing IX remote control.
 199 1: heating conductors 2: cooling circuits 3: Pt-100 sensors 4: micrometer gauge 5: detachable cover plate 6:
 200 clamping lever 7: V-seal 8: adapter tube 9: insulating sheath 10: window 11:gas inlet
 201 Connections are indicated by arrows: red for heating conductor, blue for cooling circuit, green for Pt-100 sensor
 202 and grey for nitrogen gas.

203
 204
 205 **4. Mode of operation of the stage**

206
 207 The twin-core heating conductors (1) in the lower copper block (A) and in the
 208 objective jacket (B) are connected to separate power supply units (Elektro Automatik EA-PS
 209 3150-04 B) to enable independent temperature control of the two heating/cooling elements. A
 210 cryo-thermostat (Lauda ProLine RP 845) is used to feed the two cooling circuits and provides
 211 for a constant temperature and flow rate of the cooling liquid. The stage is operated under
 212 permanent circulation of the coolant, while the temperature of the two heating/cooling

213 elements is regulated individually by varying the voltage impressed on the heating
 214 conductors. The stage reaches a maximum sample temperature that is 50°C in excess of the
 215 coolant temperature set at the thermostat. Considering the specific application to fluid
 216 inclusions in stalagmites and the use of immersion oil, a 50 °C temperature range of the stage
 217 is more than sufficient. The two Pt-100 sensors (3) attached to the lower heating/cooling
 218 block and to the microscope objective, respectively, are connected to a four-channel
 219 temperature converter (National Instruments). The temperature converter and the two power
 220 supply units are connected to a computer via USB interfaces. A LabView® based PID
 221 (Proportional-Integral-Derivative) controller is used to regulate the temperature of the two
 222 heating/cooling elements. For convenience, the stage can be operated via the function keys of
 223 a remote control (IX, Fig. 2c). A flow chart of the temperature control system is shown in Fig.
 224 3.
 225



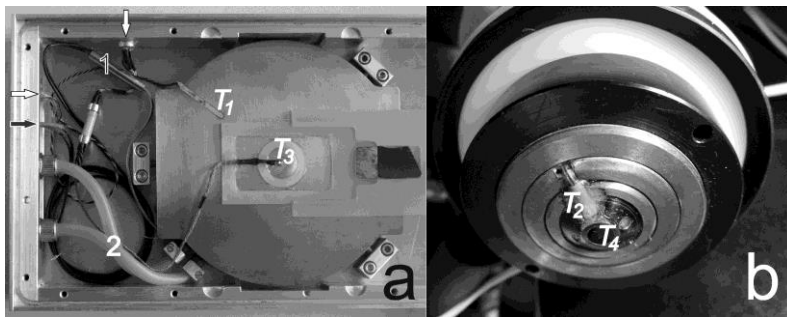
226
 227
 228 Fig. 3: Scheme of the temperature control of the heating/cooling stage. For the calibration of the stage additional
 229 Pt-100 sensors can be connected to measure the sample temperature and to monitor room temperature variations
 230 (see section below)
 231

232
 233
 234

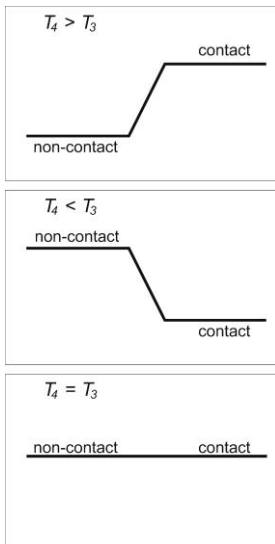
5. Thermal characterisation and temperature calibration of the stage

235 To characterise the thermal properties of the heating cooling stage such as precision,
 236 accuracy and equilibration times, we used an additional Pt-100 thin-film sensor fixed on a
 237 0.3 mm glass substrate and embedded in epoxy resin (Fig. 4a). This sensor allows us to
 238 measure the sample temperature (T_3) in the centre of the lower copper block, i.e., in the
 239 optical path of the microscope. The regular Pt-100 sensor (T_1) embedded in the lower copper
 240 block is about 40 mm off the centre, which means that T_3 is not equal T_1 due to lateral thermal
 241 gradients. The same applies for the objective temperature T_2 that is not equal to the

242 temperature of the front lens T_4 (Fig 4b). Since we cannot directly measure the sample and
 243 front lens temperatures during fluid inclusion microthermometry, we need a calibration to
 244 determine T_3 and T_4 based on the two set temperatures T_1 and T_2 . Furthermore, T_4 should
 245 equal T_3 to avoid vertical temperature gradients within the sample. We recall that the
 246 objective front lens is in contact with sample via the immersion oil. The PID controller is
 247 capable of holding T_1 and T_2 constant within ± 0.01 °C, which determines the fluctuation of T_3
 248 and T_4 .
 249



250
 251
 252 Fig. 4: Positions of temperature measurements for the stage calibration. a) T_1 : surface temperature of the copper
 253 block 40 mm apart from the sample position, measured with a permanent Pt-100 sensor. T_3 : sample temperature
 254 measured with an additional Pt-100 sensor used only for calibration. b) T_2 : objective temperature close to the
 255 front lens measured with a permanent Pt-100 sensor. T_4 : temperature of the objective front lens, not measured
 256 directly (see text for details).
 257



258
 259
 260 Fig. 5: Schematic representation of the measurement procedure used to calibrate of the objective front lens
 261 temperature T_4 by minimising the temperature gradient between T_3 and T_4 (see text for details)
 262

263 For the calibration of the stage it was not practicable to measure both the front lens
264 temperature T_4 and the sample temperature T_3 independently. Instead of measuring T_4
265 directly, we only measured T_3 as a function of T_1 and minimised the vertical temperature
266 gradient between T_3 and T_4 by adjusting the objective set temperature T_2 . In practice, we
267 measured T_3 , first, in a non-contact configuration with the objective front lens about 0.3 mm
268 above the immersion oil covering the embedded Pt-100 sensor and, subsequently, in a contact
269 configuration with the front lens immersed in the oil and thus in thermal contact with the Pt-
270 100 sensor. In this way, we were able to detect thermal gradients between the objective front
271 lens and the sample (Pt-100 sensor) on the basis of the temperature change of T_3 . By adjusting
272 the objective set temperature T_2 in repeated measurements, we finally minimised the thermal
273 gradients and thus the change of T_3 when switching over to the contact configuration. This
274 calibration procedure is illustrated schematically in Fig. 5. Calibration measurements were
275 performed at different sample temperatures T_3 and for different coolant temperatures $T_{coolant}$.
276 The results are shown in Fig. 6. The diagram displays the deviation of the two set
277 temperatures, T_1 and T_2 , from the calibrated sample temperature $T_{3(cal)}$ ($\Delta T_{set} = T_{set} - T_{3(cal)}$) as
278 function of $T_{3(cal)}$ for coolant temperatures of 0, -5, -10 and -15 °C. The relation between
279 ΔT_{set} and $T_{3(cal)}$ is nearly linear for both, the lower copper block (T_1) and the objective (T_2). To
280 test our calibration, we repeated the measurements of the sample temperature in the contact
281 configuration. Measurements were taken in 5 °C increments using a heating/cooling rate of 5
282 °C/min and an equilibration time of 15 minutes after each temperature step. Fig. 7 illustrates
283 that the deviation of the measured sample temperatures $T_{3(meas)}$ from the calibration
284 temperature $T_{3(cal)}$ is less than ± 0.02 °C, except for some measurements performed with a
285 coolant temperature of -15 °C, which show a slightly larger deviations above 15 °C. This is
286 due to the limited cooling capacity of the thermostat, which results in a slight increase of
287 $T_{coolant}$ with increasing stage temperature and larger temperature fluctuations. In addition, Fig.
288 7 indicates a small hysteresis between heating and cooling runs. Repeated measurements with
289 the same coolant temperature yield a precision (reproducibility) of T_3 of ± 0.01 °C.

290 The temperature tolerance of the Pt-100 sensors ($1/3$ Class B) used for the calibration is
291 ± 0.1 °C at 0 °C and ± 0.15 °C at 30 °C. To further improve the accuracy of the sample
292 temperature T_3 below ± 0.1 °C, we used synthetic H₂O and H₂O-CO₂ fluid inclusions for
293 absolute temperature calibrations. The use of synthetic fluid inclusions allows us to compare
294 our measurements with well-known reference temperatures, namely the melting temperature
295 of ice at 0.0 °C and the critical homogenisation of CO₂ in the H₂O- CO₂ system at 31.42 °C
296 (Morrison 1981). Measurements were performed with different coolant temperatures yielding

297 a precision of ± 0.02 °C and a slight offset of T_3 to lower temperatures: -0.1 ° at 0.0 °C and –
 298 0.15 ° at 31.42 °C. Using these offset values for a correction of the calibration, we can
 299 achieve a temperature accuracy of the heating/cooling stage of approximately ± 0.05 °C.
 300

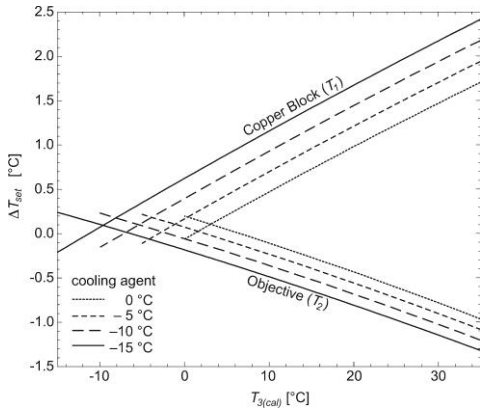


Fig 6: Deviation of the set temperatures T_1 and T_2 from the calibrated sample temperature $T_{3(cal)}$ for different coolant temperatures indicated by colours (see text for details).

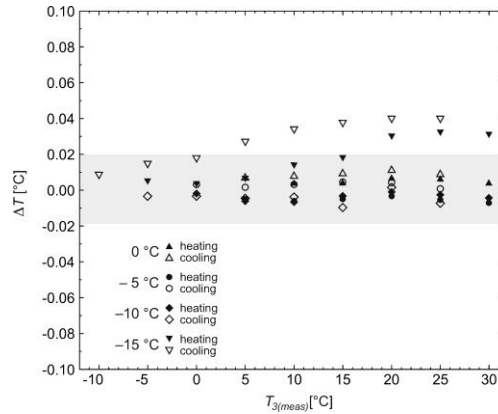


Fig. 7: Calibration check illustrating the deviation of the measured sample temperature value $T_{3(meas)}$ from the calibration $T_{3(cal)}$. Filled symbols denote measurements upon heating, open symbols upon cooling. Colours indicate different coolant temperatures.

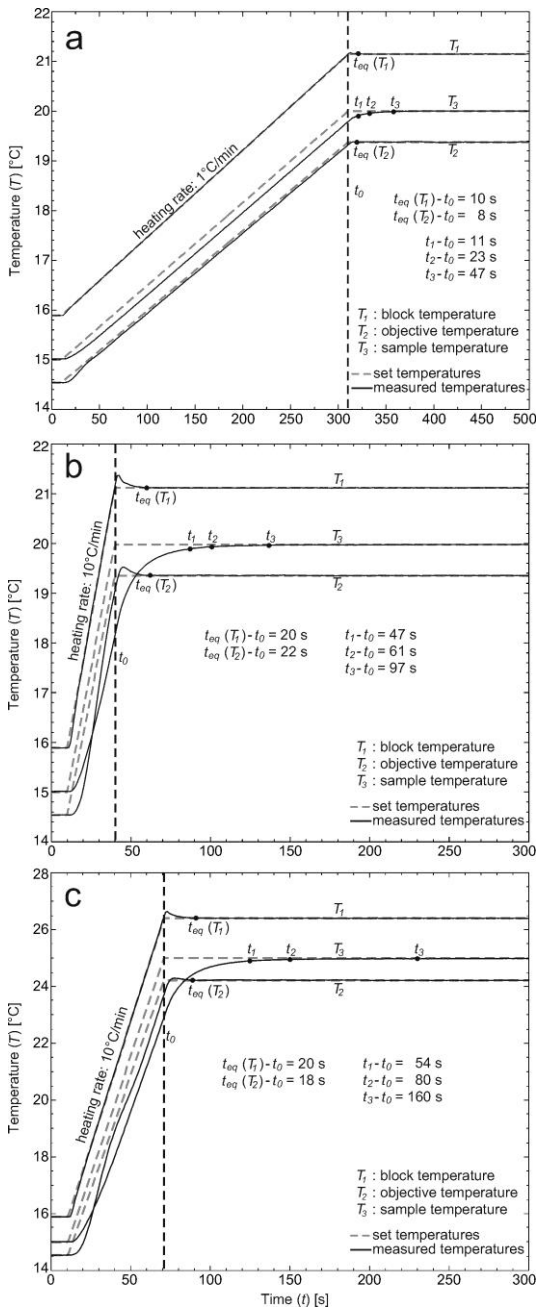
301
 302 The measurements of the ice melting temperature have also shown that absorption of
 303 light in the sample can increase T_3 by up to 0.05 °C, in spite of using a heat-absorbing IR-
 304 filter (Schott KG5 IR) in the illumination light path. In consequence of the absorption the
 305 effective sample temperature is higher than predicted by the calibration, which results in an
 306 underestimation of the ice melting temperature. To deal with this potential uncertainty we are
 307 working with a pre-defined setting of the light intensity and of the field diaphragm for sample
 308 illumination. Finally, we investigated the effect of room temperature fluctuations on the
 309 sample temperature. Both T_3 and the room temperature were measured with Pt-100 sensors.
 310 The results of these measurements indicate that a change in room temperature of 1 °C affects
 311 the sample temperature by less than 0.01 °C, which is a negligible error in an air-conditioned
 312 lab with room temperature fluctuations of less than ± 2 °C.

313 Besides precision and accuracy we also analysed the dynamic properties of the stage,
 314 namely the temperature equilibration times. The equilibration time t_{eq} denotes the time lag of
 315 the system to reach a stable temperature state after a temperature change ΔT . The time at
 316 which the set temperature reaches its new value serves as reference time t_0 . Equilibration
 317 times were measured for T_1 , the temperature of the lower heating/cooling block, for T_2 , the

318 objective temperature and for the sample temperature T_3 . Figure 8 illustrates the nominal
319 (dashed lines) and the measured temperature trends (solid lines) of T_1 , T_2 and T_3 as a function
320 of time for different temperature changes ΔT and heating rates. The diagrams show that T_1
321 and T_2 slightly over-shoot the set temperatures after heating is stopped and then return to their
322 set values. The equilibration times t_{eq} of T_1 and T_2 are very similar and depend only on the
323 heating rate (~10 s at 1 °C/min, ~20 s at 10 °C/min). The sample temperature T_3 , in contrast,
324 approaches its set temperature asymptotically from below with a considerable time lag. The
325 time the system needs to reach a stable sample temperature is too long for practical use (up to
326 360 seconds) and therefore we defined three time markers t_1 , t_2 and t_3 at which the sample
327 temperature is 0.1, 0.05 and 0.02 °C, respectively, below the final sample temperature $T_3(eq)$.
328 Fig. 8 shows that t_1 , t_2 and t_3 depend on the heating rate as well as on the temperature change
329 ΔT . With respect to fluid inclusion measurements t_1 implies a temperature overestimation of
330 0.1 °C, t_2 of 0.05 °C and t_3 of 0.02 °C. This means that the accuracy of the T_h measurements
331 also depends on the measuring routine that needs to be adjusted accordingly.

332 In practise, we use a rate of 10 °C/min to heat the stage to a temperature that is
333 approximately 2–3 °C below the expected homogenisation temperature. After an equilibration
334 time of 60-90 seconds, further heating is accomplished with a rate of 1 °C/min. Close to the
335 homogenisation, finally, when the vapour bubble becomes very small, the temperature is
336 increased stepwise in 0.05 °C increments until T_h is reached. During this last phase of the
337 measurement the sample temperature closely follows the set temperature.

338
339



340
 341
 342 Fig. 8: Temperature-time plots illustrating the equilibration times of T_1 , T_2 and T_3 after temperature increases: a)
 343 5 °C at a heating rate of 1 °C/min b) 5 °C at a heating rate of 10° C/min and c) 10 °C at a heating rate of
 344 10 °C/min. Dashed lines indicate the set temperatures and solid lines represent the measured temperature trends.
 345 The reference time t_0 denotes the end of the heat-up phase (dashed vertical line).
 346
 347

348
349
350
351
352
353
354
355
356
357
358
359
360
361
362
363
364
365
366
367
368
369
370
371
372
373
374
375
376
377
378
379
380
381
382
383
384
385
386
387
388
389
390

6. Conclusions

Liquid–vapour homogenisation of fluid inclusions in stalagmites is a promising new approach to accurately reconstruct paleotemperature variations with high temporal resolution. For this specific application, we have developed a novel heating/cooling stage for operation with large stalagmite sections and high-NA optics. With a temperature accuracy well below ± 0.1 °C and a precision of ± 0.02 °C the stage meets the requirements for fluid inclusion measurements in this temperature range. In a next step of development we will factor the dynamic properties of the stage into the PID temperature control to further reduce the equilibration times after large temperature changes and thus, to increase the efficiency of the T_h measurements.

Acknowledgements

The authors thank N. Jaussi, A. Jenk and A. Friedrich for manufacturing the components of the stage and for helpful discussions.

This work is part of the SINERGIA project “*STALCLIM – Multi-proxy climatic and environmental reconstructions from stalagmites from Switzerland, Turkey, Arabia and India*” (SNF grant: CSRI22–132646/1)

References:

Affek, H. P., Bar-Matthews, M., Ayalon, A., Matthews, A., and Eiler, J. M., 2008. Glacial/interglacial temperature variations in Soreq cave speleothems as recorded by ‘clumped isotope’ thermometry. *Geochim. Cosmochim. Ac.*, 72, 5351-5360.

Affolter, S., Fleitmann, D., and Leuenberger, M., 2014. New on-line method for water isotope analysis of speleothem fluid inclusions using laser absorption spectroscopy (WS-CRDS). *Clim. Past Discuss.*, 10, 429-467,

Fairchild, I.J., Smith, C.L., Baker, A., Fuller, L., Spötl, C., Matthey, D. and McDermott, F., 2006. Modification and preservation of environmental signals in speleothems. *Earth Sci. Rev.* 75, 105-153.

Ghosh, P., Adkins, J., Affek, H., Balta, B., Guo, W., Schauble, E.A., Schrag, D., and Eiler, J.M., 2006. ^{13}C - ^{18}O bonds in carbonate minerals: A new kind of paleothermometer. *Geochim. Cosmochim. Ac.*, 70, 1439-1456.

Kendall, A. C. and Broughton, P. L., 1978. Origin of Fabrics in Speleothems Composed of Columnar Calcite Crystals. *J. Sediment. Petrol.*, 48, 519-538.

Formatted: German
(Switzerland)

Formatted: German
(Switzerland)

- 391 Kluge, T., Marx, T., Scholz, D., Niggemann, S., Mangini, A., and Aeschbach-Hertig, W., 2008. A new tool for
 392 palaeoclimate reconstruction: Noble gas temperatures from fluid inclusions in speleothems. *Earth Planet. Sc.*
 393 *Lett.*, 269, 407-414.
 394
- 395 Krüger, Y., Stoller, P., Rička, J., and Frenz, M., 2007. Femtosecond lasers in fluid-inclusion analysis:
 396 overcoming metastable phase states. *Eur. J. Mineral.*, 19, 693-706.
 397
- 398 Krüger, Y., Marti, D., Hidalgo Staub, R., Fleitmann, D., and Frenz, M., 2011. Liquid-vapour homogenisation
 399 of fluid inclusions in stalagmites. Evaluation of a new thermometer for paleoclimate research: *Chem. Geol.*, 289,
 400 39-47.
 401
- 402 Lachniet, M.S., 2009. Climatic and environmental controls on speleothem oxygen-isotope values. *Quaternary*
 403 *Sci. Rev.*, 28(5-6), 412-432.
 404
- 405 Marti, D., Krüger, Y., Frenz, M., 2009: Fluid inclusion liquid-vapour homogenization in the vicinity of the
 406 density maximum of aqueous solutions. *ECROFI XX Abstract*
 407
- 408 Marti, D., Krüger, Y., Fleitman, D., Frenz, M., and Rička, J., 2012. The effect of surface tension on liquid-gas
 409 equilibria in isochoric systems and its application to fluid inclusions. *Fluid Phase Equilib.*, 314, 13-21.
 410
- 411 McDermott, F., 2004. Palaeo-climate reconstruction from stable isotope variations in speleothems: a review.
 412 *Quaternary Sci. Rev.*, 23, 901-918.
 413
- 414 McGarry, S., Bar-Matthews, M., Matthews, A., Vaks, A., Schilman, B. and Ayalon, A., 2004. Constraints on
 415 hydrological and paleotemperature variations in the Eastern Mediterranean region in the last 140 ka
 416 given by the delta D values of speleothem fluid inclusions. *Quaternary Sci. Rev.*, 23, 919-934.
 417
- 418 Morrison, G., 1981. Effect of water upon the critical points of carbon dioxide and ethane. *J. Phys. Chem.*, 85:
 419 759-761.
 420
- 421 Scheidegger, Y., Baur, H., Brennwald, M.S., Fleitmann, D., Wieler, R., Kipfer, R., 2010. Accurate analysis of
 422 noble gas concentrations in small water samples and its application to fluid inclusions in stalagmites. *Chem.*
 423 *Geol.*, 272, 31-39.
 424
- 425 Schwarcz, H.P., Harmon, R.S., Thompson, P., Ford, D.C., 1976. Stable isotope studies of fluid inclusions in
 426 speleothems and their paleoclimatic significance. *Geochim. Cosmochim. Ac.*, 40, 657-665.
 427
- 428 Spadin, F., Marti, D., Hidalgo Staub, R., Krüger, Y., Rička, J., Fleitmann, D., Frenz, M., *in prep.* Accuracy of
 429 stalagmite formation temperatures determined from vapour bubble radius measurements in fluid inclusions.
 430
- 431 Vonhof, H.B., van Breukelen, M.R., Postma, O., Rowe, P.J., Atkinson, T.C., Kroon, D., 2006. A continuous-
 432 flow crushing device for on-line ^7Mg H analysis of fluid inclusion water in speleothems. *Rapid Commun. Mass*
 433 *Sp.*, 20, 2553-2558.
 434
- 435 Wigley T.M.L. & Brown M.C., 1976 - The physics of caves. In: Ford T.D. & Cullingford C.H.D. (Eds.), *The*
 436 *Science of Speleology*. New York: Academic Press: 329-358.
 437
- 438 Zhang, R., Schwarcz, H. P., Ford, D. C., Schroeder, F. S., and Beddows, P. A., 2008. An absolute
 439 paleotemperature record from 10 to 6 Ka inferred from fluid inclusion D/H ratios of a stalagmite from
 440 Vancouver Island, British Columbia, Canada. *Geochim. Cosmochim. Ac.*, 72, 1014-1026.

Formatted: German
(Switzerland)